12th International Conference on Fracture Mechanics of Concrete and Concrete Structures
FraMCoS-12
B.L.A. Pichler, Ch. Hellmich, P. Preinstorfer (Eds)

https://doi.org/10.21012/FC12.1278
MS10-3:1

MESOSCALE MECHANICAL DISCRETE MODEL FOR CEMENTITIOUS COMPOSITES WITH MICROFIBERS

LEI SHEN[*], QINGWEN REN[**], GIOVANNI DI LUZIO[†] AND GIANLUCA CUSATIS[††]

[*] College of Water Conservancy and Hydropower Engineering, Hohai University,
1 Xikang Road, Nanjing 210098, China
e-mail: shenl@hhu.edu.cn

[**] Department of Enginnering Mechanics, Hohai University,
1 Xikang Road, Nanjing 210098, China
e-mail: renqw@hhu.edu.cn

[†] Department of Civil and Environmental Engineering, Politecnico di Milano,
Milan 20133, Italy
e-mail: giovanni.diluzio@polimi.it

[††] Department of Civil and Environmental Engineering, Northwestern University,
Evanston IL 60208, USA
e-mail: g-cusatis@northwestern.edu

Key words: Microfiber, Fiber reinforced concrete, Unimodal tensile strength variation, Mesoscopic discrete modeling

Abstract: Microfibers (less than 100 μm in diameter) are commonly employed in structural applications to minimize early shrinkage cracking and lower pore pressure during fires. For any application, micro fiber-reinforced concrete (FRC) structural behavior and durability must be estimated using the mechanical constitutive law. Formulating a mechanical constitutive law for FRC presents several difficulties in terms of com-prehending the physical principles and employing suitable numerical techniques. A novel model called "Lattice Discrete Particle Model for micro-FRC (LDPM-MicroF)" is presented to simulate the fracture behavior of black micro-FRC. An equivalent fiber diameter coefficient has been defined to balance modeling accuracy and computational cost so that the LDPM-MicroF model can simulate the mechanical responses of engineered cementitious composites. The unimodal variation in tensile strength caused by the increase in microfiber dose is assessed and quantitatively reproduced by LDPM-MicroF predictions.

1 INTRODUCTION

Microfibers with a diameter of less than 100 μm are widely used in two structural applications for various purposes, such as to prevent shrinkage cracking at an early age [1] and to reduce pore pressure buildup during fire incidents [2]. The mechanical constitutive law of micro fiber-reinforced concrete (FRC) is essential for estimating its structural behaviour and durability in any application. Developing a mechanical constitutive law for polymer FRC (PFRC) poses numerous challenges in terms of the physical understanding of the mechanisms and the use of appropriate numerical methods. Effective addressal of these challenges is very complex and requires a thorough understanding of the materials and processes involved. Accurately modelling the reduction in macroscopic tensile strength caused by the increased microfiber content is challenging. The models used in previous studies fail to

effectively simulate this phenomenon as they do not adequately capture the interaction mechanisms between the fibers and the matrix. In addition, the problem with the available numerical approach is that the current mesoscopic models for micro-FRCs are burdened with intolerable computational cost owing to the numerous randomly oriented fibers. To overcome these issues, this paper presents a mesoscopic discrete model for micro-FRC featuring acceptable simulation efficiency and high accuracy.

2 LDPM FOR MICROFIBER REINFORCED CONCRETE

2.1 Mesoscale discretization

The Lattice Discrete Particle Model (LDPM) [3,4] models the internal structure of concrete at the mesoscale level. This is achieved by considering the interactions between the coarse aggregates. The particle distribution is generated based on the Fuller sieve curve, which reflects the actual size distribution of the aggregates. The Delaunay tetrahedralization method effectively creates tetrahedra by connecting the centers of spherical particles. This process results in the creation of a robust lattice system formed by the edges of the tetrahedra that accurately characterizes the interactions between adjoining particles. Within the tetrahedra, the potential failure locations (12 triangular areas called "facets") are generated through a domain tessellation. As illustrated in Fig. 1, each facet has a normal vector ($\boldsymbol{n}$) and two shear vectors ($\boldsymbol{m}$ and $\boldsymbol{l}$). The concrete volume is discretized by connecting the facets surrounding each particle in a polyhedral cell system.

The numerical discretization of fiber reinforcement involves incorporating straight fibers into the concrete volume in random orientations and positions [5,6]. Each fiber was treated as a cylinder with a diameter of d_f and a length of L_f. This means that the cross-sectional area of the fiber (A_f) can be calculated as $A_\mathrm{f} = \pi d_\mathrm{f}^2/4$ and its volume (v_f) as $v_\mathrm{f} = A_\mathrm{f} L_\mathrm{f}$. Once the total fiber volume fraction V_f is known, the total number of fibers N_f in a given volume (V_sp) can be determined using the formula $N_f = \lceil V_{sp} V_f / v_f \rceil$. Here, $\lceil \cdot \rceil$ represents the ceiling function, which returns the smallest integer greater than or equal to the argument. The fiber system intersects the LDPM Cell system within the concrete volume, and one fiber can be paired with one or more facets. As shown in Fig. 1, each pair of fibers ($\boldsymbol{n}_\mathrm{f}$) and a facet ($\boldsymbol{n}$) can be divided into two embedment lengths: the shorter (L_s) and the longer (L_l). An equivalent fiber diameter coefficient ($r_\mathrm{f} = d_\mathrm{f}^\mathrm{eq}/d_\mathrm{f} \geq 1$) is defined with an equivalent fiber diameter (d_f^eq) to bridge the scale gap. The reduced number of fibers is calculated as $N_\mathrm{f}/r_\mathrm{f}^2$ when the fiber volume fraction is kept constant. The mechanical interactions between the matrix and fiber can be calculated as the fiber bridging force on the paired LDPM facet where the crack occurs.

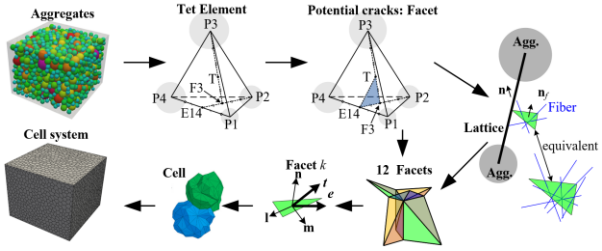

Figure 1. Mesoscale discretization of fiber reinforced concrete.

3.2 LDPM-MicroF constitutive law

The LDPM assumes mesostructural deformation with rigid body kinematics. The strain of a face attached to a tetrahedral edge (lattice element) with two particle positions $\boldsymbol{x}_i$ and $\boldsymbol{x}_j$ ($\boldsymbol{e}^\mathrm{s}$), is characterized as

$$\boldsymbol{e}^\mathrm{s} = [e_\mathrm{N}^\mathrm{s}\ e_\mathrm{M}^\mathrm{s}\ e_\mathrm{L}^\mathrm{s}]^\mathrm{T} = \left[\frac{\boldsymbol{n}^\mathrm{T}[\![\boldsymbol{u}]\!]}{l}\ \frac{\boldsymbol{m}^\mathrm{T}[\![\boldsymbol{u}]\!]}{l}\ \frac{\boldsymbol{l}^\mathrm{T}[\![\boldsymbol{u}]\!]}{l}\right]^\mathrm{T} \quad (1)$$

where e_N represents the normal component; e_M and e_L represent the two tangential components of the strain, respectively; $[\![\boldsymbol{u}]\!]$ is the displacement jump, which is calculated as the difference between the displacements at the two nodes of a facet, namely, $\boldsymbol{u}_j$ and $\boldsymbol{u}_i$, which are evaluated at the centroid of the facet; l is the distance between the two nodes, which is calculated using the Euclidean norm between the two node positions, $\|\boldsymbol{x}_j - \boldsymbol{x}_i\|_2$; $\boldsymbol{n}$ is the

unit vector, which is the normalized vector pointing in the direction from node i to node j, namely $\boldsymbol{n} = (\boldsymbol{x}_j - \boldsymbol{x}_i)/l$; $\boldsymbol{m}$ and $\boldsymbol{l}$ are two mutually orthogonal unit vectors, which are defined in such a way that they are orthogonal to $\boldsymbol{n}$. The translational and rotational degrees of freedom of the particles were used to calculate the displacements $\boldsymbol{u}_i$ and $\boldsymbol{u}_j$ through rigid-body kinematics.

The elastic behavior of the LDPM assumes that the tractions of the solid skeleton, represented by $\boldsymbol{t}^{\mathrm{s}}$, are proportional to the corresponding strains as follows:

$$\boldsymbol{t}^{\mathrm{s}} = [t_{\mathrm{N}}^{\mathrm{s}}\ t_{\mathrm{M}}^{\mathrm{s}}\ t_{\mathrm{L}}^{\mathrm{s}}]^{\mathrm{T}} = [E_{\mathrm{N}} e_{\mathrm{N}}^{\mathrm{s}}\ E_{\mathrm{T}} e_{\mathrm{M}}^{\mathrm{s}}\ E_{\mathrm{T}} e_{\mathrm{L}}^{\mathrm{s}}]^{\mathrm{T}} \quad (2)$$

where $t_{\mathrm{N}}^{\mathrm{s}}$, $t_{\mathrm{M}}^{\mathrm{s}}$, and $t_{\mathrm{L}}^{\mathrm{s}}$ represent the normal and shear components of the traction; $E_{\mathrm{N}} = E_0$ and $E_{\mathrm{T}} = \alpha E_0$, where E_0 denotes the effective normal elastic modulus and $\alpha = 0.25$ is the shear-normal coupling parameter of concrete, as mentioned in a previous study. In addition, the mesoscopic crack-opening vector ($\boldsymbol{\delta}$) in each LDPM facet is determined as follows:

$$\boldsymbol{\delta} = \delta_{\mathrm{N}}\boldsymbol{n} + \delta_{\mathrm{L}}\boldsymbol{l} + \delta_{\mathrm{M}}\boldsymbol{m} \quad (3)$$

where $\delta_{\mathrm{N}} = l(e_{\mathrm{N}}^{\mathrm{s}} - t_{\mathrm{N}}^{\mathrm{s}}/E_{\mathrm{N}})$ is the crack opening in the normal direction, and $\delta_{\mathrm{L}} = l(e_{\mathrm{L}}^{\mathrm{s}} - t_{\mathrm{L}}^{\mathrm{s}}/E_{\mathrm{L}})$ and $\delta_{\mathrm{M}} = l(e_{\mathrm{M}}^{\mathrm{s}} - t_{\mathrm{M}}^{\mathrm{s}}/E_{\mathrm{M}})$ are two shear slidings of the crack in directions $\boldsymbol{m}$ and $\boldsymbol{l}$. As soon as a crack open (i.e., $\delta \geq 0$), the fiber crack-bridging force begins to contribute to the paired facet. It was assumed that this force acts parallel to the stress on the LDPM solid skeleton (matrix). As the main innovation of this work, the facet traction is the sum of the bridging forces of the fibers with a section area (A_{f}) within the facet area (A_{F}) and the cohesion of the matrix with the area ($A_{\mathrm{F}} - A_{\mathrm{f}}$). To determine the overall stress on each facet of the LDPM, the total stress ($\boldsymbol{t}$) can be calculated as follows:

$$\boldsymbol{t} = \left(1 - \frac{A_{\mathrm{f}}}{A_{\mathrm{F}}}\right)\boldsymbol{t}^{\mathrm{s}} + \sum_{\mathrm{fiber}\in A_{\mathrm{F}}}\left(\frac{\boldsymbol{P}_{\mathrm{f}}}{A_{\mathrm{F}}}\right) \quad (4)$$

where A_{F} is the LDPM facet area; $\boldsymbol{P}_{\mathrm{f}}$ is the fiber bridging force of a single fiber on the paired facet; $A_{\mathrm{f}} = \sum_{\mathrm{fiber}\in A_{\mathrm{F}}}(\pi d_{\mathrm{f}}/4\cos\theta)$ is the total intersection area of fibers crossing this facet (d_{f} is the fiber diameter and θ is the angle between fiber and facet). As discussed, $\boldsymbol{P}_{\mathrm{f}} \approx 0$ represents the facet under compression ($e_{\mathrm{N}}^{\mathrm{s}} < 0$) or with no crack opening ($\delta = 0$).

Each fiber bonded to the matrix is straight and elastic with negligible bending stiffness. An embedded fiber must first detach completely from the surrounding matrix to achieve a pure frictional pullout. During the debonding stage, a "tunnel-type" cracking process occurs, which is characterized by a bond fracture energy of G_{d} , and a bond frictional stress of τ_0. The critical slippage, v_{d}, which represents complete detachment, can be expressed as follows:

$$v_{\mathrm{d}}^{\mathrm{eq}} = \frac{2\tau_0^{\mathrm{eq}} L_{\mathrm{e}}^2}{E_{\mathrm{f}} d_{\mathrm{f}}^{\mathrm{eq}}} + \left(\frac{8 G_{\mathrm{d}}^{\mathrm{eq}} L_{\mathrm{e}}^2}{E_{\mathrm{f}} d_{\mathrm{f}}^{\mathrm{eq}}}\right)^{\frac{1}{2}} \quad (5)$$

where L_{e} is the length of the fiber embedding, and E_{f} is the fiber elastic modulus. The superscript "eq" denotes an equivalent value that provides the same contribution as the original value but refers to the equivalent fiber diameter. The equivalent fiber diameter, denoted as $d_{\mathrm{f}}^{\mathrm{eq}} = r_{\mathrm{f}} d_{\mathrm{f}}$, was defined to reduce the number of microfibers while keeping the fiber length constant. Similarly, the equivalent bond fracture energy, $G_{\mathrm{d}}^{\mathrm{eq}} = r_{\mathrm{f}} G_{\mathrm{d}}$, and the equivalent bond frictional stress, $\tau_0^{\mathrm{eq}} = r_{\mathrm{f}}\tau_0$, are defined. By substituting the values of $d_{\mathrm{f}}^{\mathrm{eq}}$, $G_{\mathrm{d}}^{\mathrm{eq}}$, and τ_0^{eq} into Eq. (5), the equivalent critical slippage, $v_{\mathrm{d}}^{\mathrm{eq}} = v_{\mathrm{d}}$, is determined, which is independent of the equivalent coefficient r_{f}.

At the debonding stage ($v < v_{\mathrm{d}}$) of an equivalent fiber, the bridging force ($P^{\mathrm{eq}}(v)$) can be calculated by:

$$P^{\mathrm{eq}}(v) = \left[\frac{\pi^2 E_{\mathrm{f}} (d_{\mathrm{f}}^{\mathrm{eq}})^3}{2}\left(\tau_0^{\mathrm{eq}} v + G_{\mathrm{d}}^{\mathrm{eq}}\right)\right]^{\frac{1}{2}} \quad (6)$$

At the pull-out stage ($v > v_{\mathrm{d}}$), the fiber resistance is exclusively friction, and the bridging force of an equivalent fiber is calculated as follows:

$$P^{\mathrm{eq}}(v) = P_0^{\mathrm{eq}}\left(1 - \frac{v - v_{\mathrm{d}}}{L_{\mathrm{e}}}\right)\left(1 + \beta^{\mathrm{eq}}\frac{v - v_{\mathrm{d}}}{d_{\mathrm{f}}^{\mathrm{eq}}}\right) \quad (7)$$

where P_0^{eq} is the initial equivalent fiber load given by $P_0^{\mathrm{eq}} = \pi L_{\mathrm{e}} d_{\mathrm{f}}^{\mathrm{eq}} \tau_0^{\mathrm{eq}}$, and $\beta^{\mathrm{eq}} = r_{\mathrm{f}}\beta$ (β is the slip hardening–softening) is the equivalent dimensionless coefficient that determines the friction between fiber and tunnel as shown in Fig. 2. For reloading, the $P^{\mathrm{eq}} = 0$ since the soft microfiber is studied.

The friction coefficient does not change with the slippage in the case of $\beta^{\mathrm{eq}} = 0$. For the case of $\beta^{\mathrm{eq}} < 0$ or $\beta^{\mathrm{eq}} > 0$, the interfacial friction decreases or increases with the slippage. When the equivalent parameters are substituted into Eqs. (6) and (7), the bridging force of one equivalent fiber contributes the same as r_{f}^2 microfibers, being $P^{\mathrm{eq}}(v) = r_{\mathrm{f}}^2 P(v)$.

The force and moment equilibrium of each fiber-reinforced LDPM cell complete the governing equation. This is expressed as:

$$\sum_{k\in\mathcal{F}_I} A_k^{\mathrm{p}}\,\boldsymbol{t}_k + V_I\boldsymbol{b} = \boldsymbol{0}, \sum_{k\in\mathcal{F}_I} A_k^{\mathrm{p}}\,\boldsymbol{c}_k \times \boldsymbol{t}_k = \boldsymbol{0} \quad (8)$$

where $\boldsymbol{t}_k$ is facet k stress; $\mathcal{F}_I$ includes all facets surrounding cell I; $A_k^{\mathrm{p}} = A_k \boldsymbol{n}_{\mathrm{L}}^{\mathrm{T}} \boldsymbol{n}_k$ is the projected area of facet k, where $\boldsymbol{n}_k$ is the normal unit vector of facet k with area A_k, and $\boldsymbol{n}_{\mathrm{L}}$ is the orientation of LDPM tetrahedron edge associated with facet k; V_I is the cell volume; $\boldsymbol{b}$ is the external body forces on cell; $\boldsymbol{c}_k$ represents the distance between facet k and the cell center.

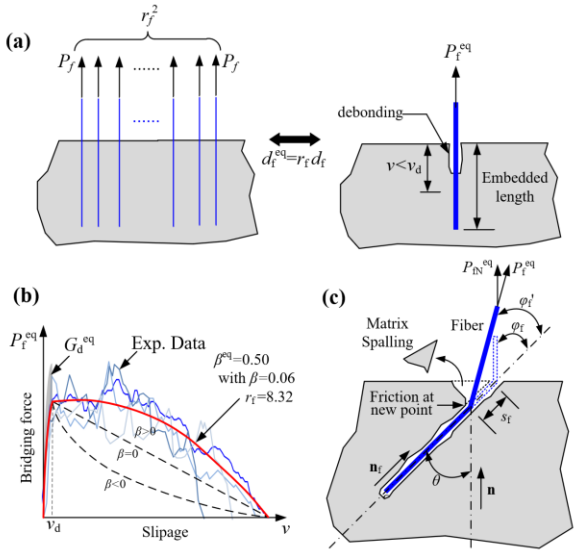

Figure 2. Illustrations of fiber–matrix interaction. (a) Pullout friction and slippage; (b) calibration of β^{eq} [7]; (c) matrix spalling.

3 MODEL CAPABILITY: FOUR-POINT BENDING TEST

In this section, simulations of the four-point bending tests of micro-basalt FRC (BFRC) [8] are conducted to demonstrate the model's ability to reproduce the observed cracking patterns. The bending test, according to the Chinese test standard (GB/T50081—2019), can effectively capture the variations in cracking patterns caused by the addition of fibers.

The tested beams had a square cross-section of 100 mm depth × 100 mm height and a length of 400 mm. The specimen was securely supported by two steel rods, each with a span of 300 mm, and the load was applied using two additional steel rods with a span of 100 mm. The numerical setup reproduced the experimental setup identically, as shown in Fig. 3. The steel rods and specimen were adjusted so that there is high friction between them. The friction is characterized by a friction coefficient, denoted as μ. It is described as a function of the contact slippage (s) and expressed in the form of $\mu(s) = \mu_{\mathrm{d}} + (\mu_{\mathrm{s}} - \mu_{\mathrm{d}})s_0/(s + s_0)$. Here, μ_{s} is equal to 0.13, μ_{d} is equal to 0.015, and s_0 is equal to 1.3 mm.

To reduce the computational cost, only the potential area of damage shown in Fig. 3(b) was modeled with the LDPM-MicroF, and the elastic FEM models the remaining parts with an elastic modulus of 20 GPa. The coarse aggregates with a diameter of 5–20 mm and the micro-basalt fiber with a diameter of 16 μm and length of 30 mm are used in the discretization of the material as shown in Fig. 3(b). The value $r_{\mathrm{f}} = 6$ was adopted to obtain an average facet–fiber intersection of eight within the potential damage area.

3.1 Effectiveness of the model

Unimodal strength variation was also observed in this experimental investigation (Fig. 3(a)). The flexural strength increases from 5.20 to 5.81 MPa, when the fiber volume fraction is increased up to 0.2%.

When the fiber volume fraction is increased to 0.3%, the flexural strength decreases to 5.6 MPa, which is lower than the flexural strength of the mix with V_{f} = 0.1%. The model parameters for plain concrete were first calibrated by modeling the tests on the matrix. Subsequently, the parameters of the fiber–matrix interaction were calibrated by modeling the mixture with a volume fraction of 0.1% of microfibers. These results are

summarized in Table 1. Third, numerical simulations of the mixes with 0.2% and 0.3% volume fractions of microfibers were performed as pure predictions.

As shown in Fig. 3(a), the post-peak curves of loading displacement versus flexural stress differed significantly. The specimens made of plain concrete exhibit brittle failure. The residual bearing stress increased with the fiber dosage. When the fiber volume fraction reached 0.3%, the post-peak bearing stress gradually increased with the bending displacement and then reached a second stress peak. The mixture with V_f = 0.3% exhibits apparent ductile failure. The increase in the post-peak bearing stress also represents an increase in the material fracture energy. This phenomenon can also be observed visually by comparing the cracking patterns illustrated in Fig. 3(b). Interestingly, the four-point bending test without a notch is suitable to confirm the ability of the model to reproduce cracking patterns (failure mode). The presence of micro-basalt fibers significantly increases the number of microcrack initiations in the bending area and can also change the macrocrack path. The case of $V_f = 0.3\%$ with r_f = 3 (average facet–fiber intersection of 12) was also investigated to check the sensitivity to r_f. By comparing the flexural stress variations for the cases with r_f = 3 and r_f = 6, it is clear that increasing r_f from 3 to 6 shows a good agreement in the flexural strength and post-peak bearing stress and significantly reduces the simulation time from 18 to 4 h (CPU i9-13900K with 12 threads).

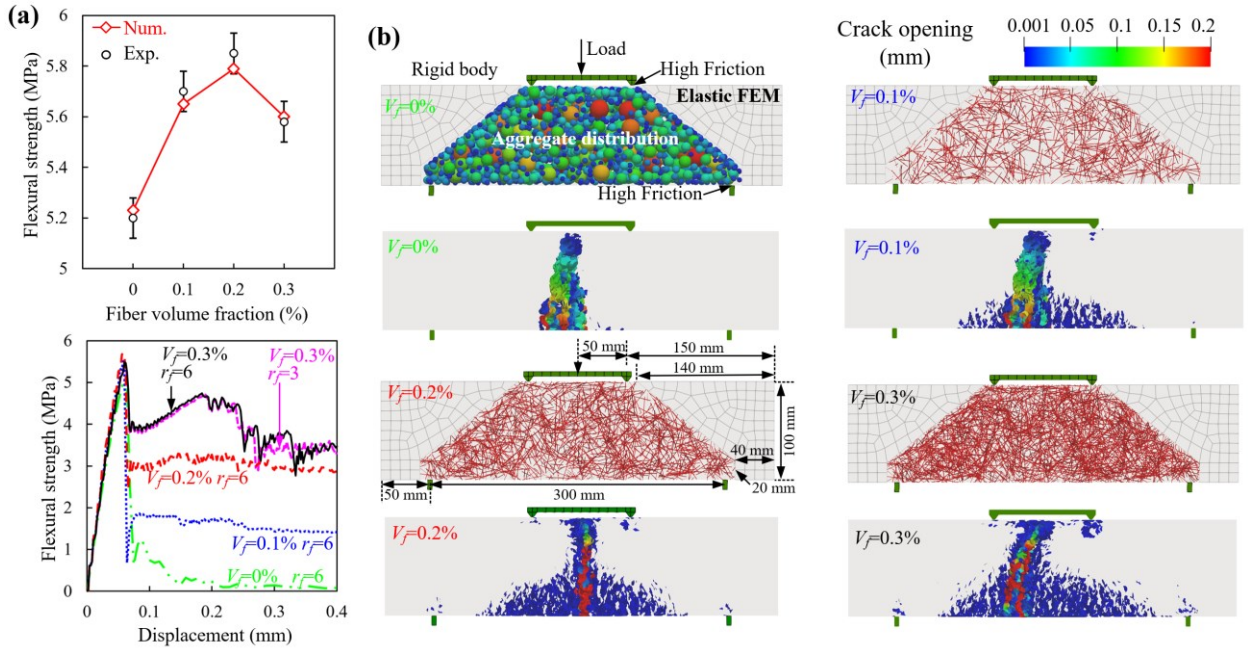

Figure 3. Results of the four-point bending tests of BFRC [8]. (a) Flexural strength and stress–strain curve; (b) model setups and cracking patterns. Num.: numerical data; FEM: finite element method.

3.2 Effect of the parameters in the fiber–matrix bond law

The effect of mechanical parameters describing fiber–matrix interaction on the macroscopic behavior (i.e., flexural stress versus displacement curves) is investigated by considering the influence of the fiber–matrix bond frictional stress (τ_0), the slip hardening-softening (β), fiber elastic modulus (E_f), and fiber tensile strength (σ_{uf}). The fiber elastic modulus and tensile strength were assumed to be constant. This paper examines a variety of scenarios with fiber–matrix bond stress τ_0 ranging from 0.1 to 1 MPa, and the fiber–matrix slip hardening-softening β ranging from −0.05 to 0.05. The results for these cases are shown in Fig. 4.

In Fig. 4(a), the fiber–matrix bond stress τ_0 significantly increases the post-peak stress but only has a marginal effect on the peak stress. This phenomenon can also be explained by larger FPZ and denser microcracks at $\tau_0 = 1$ MPa than in the case of $\tau_0 = 0.1$. The observed condition was primarily a consequence of the basic assumption of the model, which states that the fiber bridging force was active during crack initiation. Interestingly, the results in Fig. 4(b) show a surprising trend: increasing the bond stress does not always lead to improved mechanical responses, as shown by the comparison between the cases with $\tau_0 = 1$ and 0.5 MPa. The flexural stress shows a remarkable decrease owing to fiber breakage when the fiber bridging force exceeds its tensile strength. With the development of loading, the post-peak stress may drop below the case with a smaller value of the fiber–matrix bond stress.

The fiber–matrix slip hardening–softening depends on the fiber surface treatment, fiber type, fiber material, and matrix mixture. The parameter can be determined from the fiber pull-out test data. Our results in Fig. 4(b) reveal that an increase in fiber–matrix slip hardening–softening β leads to a slight rise in post-peak bearing stress and a distinct mesoscopic cracking pattern. Therefore, the recommended slip hardening–softening is zero if the fiber pull-out test is not available.

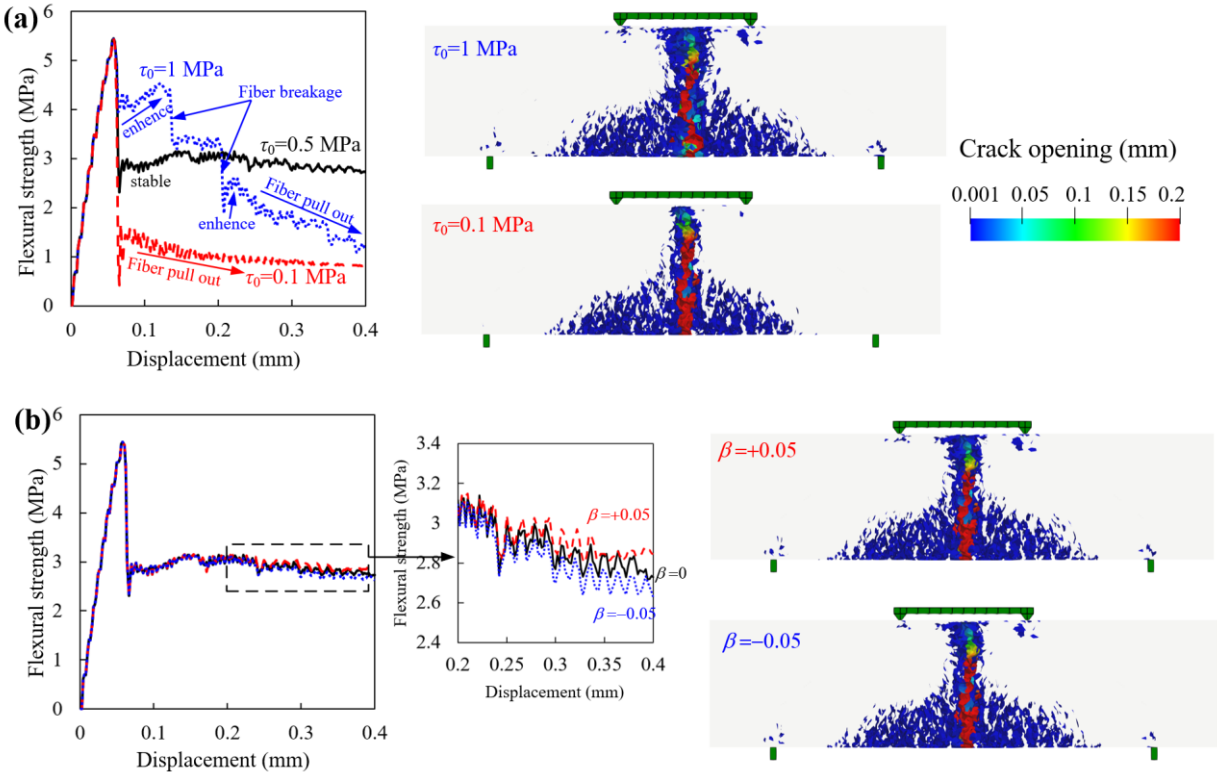

Figure 4. Effect of the mechanical parameters describing the fiber–matrix interaction. (a) Fiber–matrix bond stress τ_0; (b) fiber–matrix slip hardening-softening β.

4 CONCLUSIONS

This study presented groundbreaking innovations in the numerical efficiency of mesoscale approaches, specifically in the context of microFRC. These innovations have significantly improved the accuracy and speed of numerical simulations. In addition, this research has yielded fresh perspectives on the physical understanding of the mechanical properties of micro-FRC, which consequently holds significant ramifications for the field of study.

The LDPM-MicroF model solves the computational challenge posed by the enormous number of microfibers (diameter ≤ 100 μm) by defining an equivalent coefficient

for fiber diameter. To ensure high modeling accuracy and numerical efficiency, it was determined that the equivalent coefficient of the fiber diameter must be set appropriately to guarantee a minimum average of fiber–matrix intersection equal to 4.

LDPM-MicroF can predict the initial increase and subsequent decrease in tensile strength of micro-FRC as the microfiber content increases. This capability is due to the model's ability to account for the combined effects of the weakened fiber contribution at the mesoscale and the positive contribution of the nearby matrix at the microscale. From a mesoscopic mechanical standpoint, the microfibers contribute less to the material resistance than the replaced matrix. Therefore, the presence of microfibers leads to a reduction in macroscopic tensile strength at each microfiber dose. In the constitutive relationships, the areas of fiber intersection and effective matrix on the crack surfaces were distinguished to simulate this phenomenon. The presence of microfibers in a cementitious composite can slightly increase the strength of the nearby matrix. This is due to the "near-field effect" of the microfibers, which increases the strength of the matrix in the presence of many fibers. This phenomenon was accounted for by relating the facet tensile strength of the matrix to the fiber content.

REFERENCES

[1] Banthia N, Gupta R., 2006. Influence of polypropylene fiber geometry on plastic shrinkage cracking in concrete. *Cement Concr Res*. **36**(7):1263–7.

[2] Shen L., Yao X., Di Luzio G., Jiang M., Han Y., 2023. Mix optimization of hybrid steel and polypropylene fiber-reinforced concrete for anti-thermal spalling. *J Build Eng*. **63**:105409.

[3] Cusatis G., Pelessone D., 2011. Mencarelli A. Lattice discrete particle model (LDPM) for failure behavior of concrete. I: theory. *Cement Concr Compos*. **33**(9):881–90.

[4] Cusatis G., Mencarelli A., Pelessone D., Baylot J., 2011. Lattice discrete particle model (LDPM) for failure behavior of concrete. II: calibration and validation. *Cement Concr Compos*. **33**(9):891–905.

[5] Schauffert EA., Cusatis G., 2011. Lattice discrete particle model for fiber-reinforced concrete. I: theory. *J Eng Mech*. **138**(7):826–33.

[6] Schauffert EA., Cusatis G., Pelessone D., O'Daniel JL., Baylot JT., 2011. Lattice discrete particle model for fiber-reinforced concrete. II: tensile fracture and multiaxial loading behavior. *J Eng Mech*. **138**(7):834–41.

[7] Maida PD., Radi E., Sciancalepore C., Bondioli F., 2015. Pullout behavior of polypropylene macro-synthetic fibers treated with nano-silica. *Constr Build Mater*. **82**:39–44

[8] Li T., Zhang X., Liu H., Fan Z., Chen C., 2020. Experimental research on mechanical properties of hybrid fiber concrete after high temperature. *J Railway Sci Eng*. **17**(5):1171–7.